

1 **Water Incorporation Mechanisms and Effects in MgSiO₃-majorite Under High**
2 **Temperature and Pressure Conditions**

3
4 **Yancheng Lou^{1,2,3,*}, Zhigang Zhang^{3,4}, Andrew M. Walker⁵, Stephen Stackhouse⁶, Meng**
5 **Chen^{1,2}, and Hongping He^{1,2,4}**

6 ¹State Key Laboratory of Deep Earth Processes and Resources, Guangzhou Institute of
7 Geochemistry, Chinese Academy of Sciences, Guangzhou, 510640, China.

8 ²Guangdong Research Center for Strategic Metals and Green Utilization, Guangzhou, 510640,
9 China.

10 ³Key Laboratory of Planetary Science and Frontier Technology, Institute of Geology and
11 Geophysics, Chinese Academy of Sciences, Beijing 100029, China.

12 ⁴College of Earth and Planetary Sciences, University of Chinese Academy of Sciences, Beijing
13 100049, China.

14 ⁵Department of Earth Sciences, University of Oxford, South Park Road, Oxford OX1 3AN, United
15 Kingdom.

16 ⁶School of Earth and Environment, University of Leeds, Leeds LS2 9JT, United Kingdom.

17

18 Corresponding author: Yancheng Lou (louyancheng@gig.ac.cn)

19

20 **Key Points:**

- 21
- The dominant water incorporation mechanisms in MgSiO₃-majorite are the two types of tetrahedral hydrous defects.
 - The impact of the two dominant tetrahedral hydrous defects on the elastic properties of MgSiO₃-majorite are significantly different.
 - In MgSiO₃-majorite, water incorporation exhibits a greater effect on S-wave than on P-wave velocities under high-pressure conditions.
- 22
23
24
25
26

* Corresponding author: louyancheng@gig.ac.cn

27 **Abstract**

28 The incorporation of water in high-pressure minerals is essential for the water cycle within the
29 interiors of terrestrial planets. Majoritic garnet, a major component in the mantles of Earth and
30 Mars, plays a significant role in this context. In this study, we use first-principles simulations to
31 explore water incorporation mechanisms in MgSiO₃-majorite, which is a key end-member of
32 majoritic garnet, at conditions up to 2000 K and 20 GPa. By dealing with the relationship between
33 chemical potential and the Gibbs free energy changes for the reactions at equilibrium conditions,
34 we determine the ratios of the seven potential hydrous defects. Our results reveal that the Si₂ and
35 Si₃ defects, which are of the hydrogarnet-type, dominate water incorporation in MgSiO₃-majorite.
36 In addition, we evaluate the effects of these hydrous defects on seismic wave velocities. The
37 presence of Si₂ and Si₃ defects, with an expected water concentration of ~700 ppm, has a small
38 effect on both P-wave and S-wave velocities. Nevertheless, the influence of water on lateral
39 variations in the seismic wave velocities of MgSiO₃-majorite, which is opposite to that found for
40 ringwoodite, offers a potential tool for investigating compositional heterogeneities in hydrated
41 regions of planetary mantles.

42

43 **Plain Language Summary**

44 Water in high-pressure minerals makes up a significant component of deep water in terrestrial
45 planets and plays an important role in their planetary water cycles. Constraining how water is
46 stored in majoritic garnet, a major mineral in the mantles of Earth and Mars, is important for
47 understanding how water is stored and moves in these environments. In this study, we explore how
48 water is incorporated into MgSiO₃-majorite, a key end-member of majoritic garnet, under high-
49 pressure and high-temperature conditions. Based on extensive first-principles simulations, we find
50 that two types of tetrahedral hydrous defects are the main ways water is stored in MgSiO₃-majorite.
51 These defects have a small effect on the seismic velocities of MgSiO₃-majorite at an expected
52 water concentration of ~700 ppm. However, they exhibit a stronger influence on S-wave than on
53 P-wave velocities, which is similar to the behavior observed in wadsleyite but different from that
54 in ringwoodite. This characteristic may help us to better understand compositional heterogeneities
55 in hydrated regions of planetary mantles.

56

57 **1 Introduction**

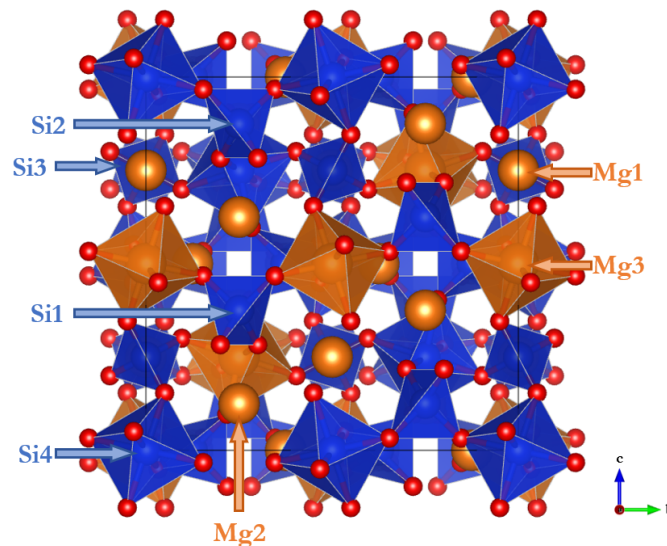
58 Water is important for shaping the evolution of terrestrial planets such as Earth and Mars (Bell
59 & Rossman, 1992; Bolfan-Casanova, 2005; Nestola & Smyth, 2016; Ni et al., 2017; Ohtani, 2020;
60 Pearson et al., 2014; Peslier et al., 2017; Smyth & Jacobsen, 2006). The presence of water can
61 significantly affect the melting point, wave speed, thermal conductivity, electrical conductivity,
62 and other properties of minerals (Faccenda, 2014; Mao & Li, 2016; B. Zhang & Xia, 2021). In
63 view of this, it is necessary to investigate the mechanism of water incorporation in high-pressure
64 minerals, to better understand the influence of water.

65 Majoritic garnet, the high-pressure phase of garnet, is a major component in the mantles of
66 Earth and Mars (van der Lee, 2023; Yoshizaki & McDonough, 2020, 2021). It is the second most
67 abundant component (up to ~40 mol.%; Frost, 2008; Yoshizaki & McDonough, 2021) in the
68 Earth's mantle transition zone (MTZ) and the major component (up to ~90 mol.%; Smith et al.,

69 2018; Stixrude & Lithgow-Bertelloni, 2012) in cold slabs at Earth's MTZ depth. In the mantle of
 70 Mars, it is the second most abundant component (up to ~40 mol.%; Yoshizaki & McDonough,
 71 2020, 2021) at depths of about 1000-1800 km. Majoritic garnet not only plays significant roles in
 72 many geodynamic processes, but also acts as an important reservoir and carrier of water in the
 73 deep interiors of these planets (Scambelluri et al., 2008; van Mierlo et al., 2013).

74 MgSiO₃-majorite (space group: I4₁/a, abbreviated as Mgmj hereafter) is a key silicon-rich
 75 end-member of majoritic garnet (Akaogi & Akimoto, 1977; Angel et al., 1989; Irifune, 1987;
 76 Irifune & Ringwood, 1987; Ringwood, 1967, 1991). As shown in Fig.1, its crystal structure
 77 features seven types of polyhedrons, marked as Mg1-3 and Si1-4, which is more than other garnet
 78 end-members because of the occupation of octahedral sites by equal amounts of Si⁴⁺ and Mg²⁺
 79 instead of trivalent cations. Mg1 and Mg2 polyhedrons are dodecahedrons which are distinguished
 80 by distortion relative to the cube (Mg1 is more distorted than Mg2). Mg3 and Si4 are octahedrons
 81 whose main difference is the type of central cations. Si1, Si2, and Si3 are tetrahedrons which
 82 mainly differ in their bonding environment, they connect with four Mg octahedrons, four Si
 83 octahedrons, and two Mg and two Si octahedrons, respectively. These polyhedrons provide
 84 multiple possible incorporation mechanisms for water because hydrous defects (hydroxyl point
 85 defects) in nominally anhydrous minerals, which are generated by the substitution of H for metal
 86 cations minerals, are the main storage mechanism of water (Bell & Rossman, 1992; Hirschmann
 87 & Kohlstedt, 2012; Inoue et al., 1998; Jacobsen, Jiang, et al., 2008; Manghnani et al., 2005; Mao
 88 et al., 2011; Peslier et al., 2017; Walker et al., 2007; Wang et al., 2006).

89



90

91 **Figure 1.** Unit cell of MgSiO₃-majorite, which is a tetragonal structure (space group: I4₁/a) with
 92 160 atoms (Mg₃₂Si₃₂O₉₆) and includes eight Mg₃(Mg,Si)[SiO₄]₃ units. Red balls represent O²⁻;
 93 Orange balls represent Mg²⁺ (the exposed balls represent Mg²⁺ in Mg1 and Mg2 dodecahedral
 94 sites, the balls in orange octahedrons represent Mg²⁺ in Mg3 sites); Blue balls represent Si⁴⁺ (the
 95 balls in blue tetrahedrons and octahedrons represent Si⁴⁺ in Si1-3 and Si4 sites, respectively).

96

97 Previous studies of water incorporation mechanisms in Mgmj are limited to static results
 98 (Pigott et al., 2015), which found the Si2 hydrous defect to be the dominant water incorporation
 99 mechanism at MTZ pressures. This type of hydrous defect, together with Si1 and Si3 defects,
 100 where four hydrogen atoms replace a silicon atom in a tetrahedral site, are known as “hydrogarnet
 101 defects” (Cohen-Addad et al., 1967) and are common in natural garnets and other minerals at
 102 relatively low temperatures (Balan et al., 2011; Blanchard et al., 2009; Qin et al., 2018; Wright et
 103 al., 1994). There is even a complete solid solution sequence called hydrogrossular,
 104 $\text{Ca}_3\text{Al}_2(\text{SiO}_4)_{3-x}(\text{OH})_{4x}$, in which all the Si tetrahedrons become hydrous defects (Adhikari et al.,
 105 2017; Rossman & Aines, 1991). However, the water incorporation mechanism may change at
 106 higher temperatures, as found for other mantle minerals. For instance, the main water incorporation
 107 mechanism of forsterite changes from Si tetrahedral defects to Mg octahedral defects with
 108 increasing temperature (Qin et al., 2018; Walker et al., 2007). Motivated by these previous studies,
 109 we deployed first-principles simulations of Mgmj and inspected its seven potential hydrous defects
 110 up to 2000 K and 20 GPa. By solving the equations for the chemical potential and the Gibbs free
 111 energy changes for the reactions at equilibrium conditions, we obtained their ratios that quantify
 112 the main incorporation mechanisms of water. In addition, we further calculated the elastic
 113 properties of dry and hydrous Mgmj to show the impact of hydrous defects on its physical
 114 properties and discussed the implications of our results.

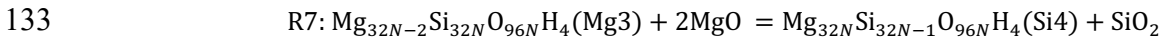
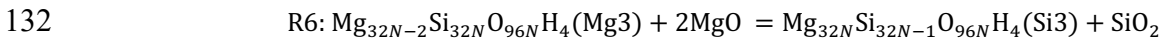
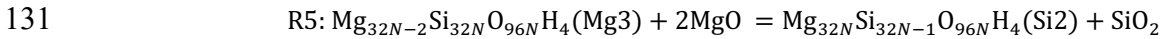
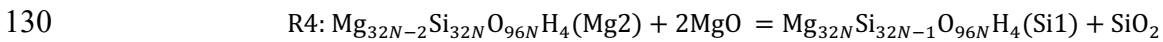
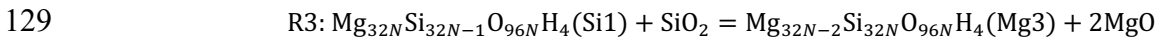
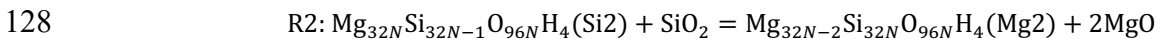
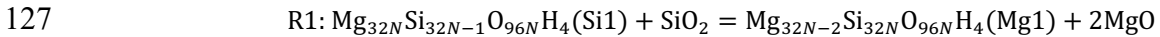
115

116 2 Methods and computational details

117 In order to understand the distribution of hydrogen between the different types of possible
 118 hydrous defect in Mgmj, we need a model for the free energy change of reactions amongst the
 119 defect types and data on the relative enthalpy and entropy of the defects. We first introduce our
 120 model of reactions before describing the atomic scale approach we use to investigate individual
 121 defects.

122 2.1 Reaction model

123 Since Mgmj has seven types of cation site, the incorporation of water may involve equilibria
 124 among these potential cation defects and water. To avoid the difficulty of directly modeling the
 125 energetics of supercritical water, we evaluate the relative stability of every pair of defect
 126 mechanisms by the following reactions (Pigott et al., 2015):



134 where the symbols Mg1-3 and Si1-4 represent corresponding hydrous defects in Mgmj, the N
 135 represents the number of unit cells of dry Mgmj corresponding to the hydrous Mgmj phases, the
 136 phase MgO is periclase, the phase SiO_2 is alpha-quartz at 0 K and 0 GPa but stishovite at 0 K and
 137 10 and 20 GPa as well as at 2000 K and ~20 GPa. We treat MgO and SiO_2 as precipitates and

138 consider the other reactants and products of hydrous Mgmj phases as a solid binary mixture, which
 139 means their chemical potential are (Levine, 2009):

$$140 \quad \mu_i = \mu_i^* + RT \ln x_i \gamma_i \quad (1)$$

141 where μ_i is the chemical potential of component i with mole fraction x_i at temperature T and
 142 pressure P , R represent the gas constant, γ_i represent the activity coefficient which can be treated
 143 as 1 because of the similar structure between hydrous Mgmj phases, and μ_i^* is the chemical
 144 potential of pure i (phase of hydrous Mgmj) at the same temperature and pressure. For reactions
 145 above, taking R1 as an example, we have:

$$146 \quad \Delta_r G = \sum v_i \mu_i^* + RT \ln \frac{x_{\text{Mg1}}}{x_{\text{Si1}}} \quad (2)$$

147 where $\Delta_r G$ is the Gibbs free energy change of reaction, v_i is the stoichiometric number, the
 148 subscripts of Mg1 and Si1 represent the phase of hydrous Mgmj with two Mg1 hydrous defects
 149 and one Si1 hydrous defect, respectively. $\sum v_i \mu_i^*$ can be given by:

$$150 \quad \sum v_i \mu_i^* = \sum v_i [H_i^* - T(S_{i,\text{vib.}}^* + S_{i,\text{conf.}}^*)] \quad (3)$$

151 where H_i^* is the enthalpy of pure i , which is obtained as $U + pV$ from molecular dynamics within
 152 the NVT ensemble. Here, U is the ensemble-averaged internal energy, p is target pressure (rather
 153 than the ensemble-averaged pressure, as explained in Section S1.2), and V is the volume, which is
 154 constant. Notably, the enthalpy of the pure hydrous Mgmj phase with different water
 155 concentrations ($H_{\text{hydrous Mgmj}}^*$) is calculated from the enthalpy of pure Mgmj (H_{Mgmj}^*) and the
 156 hydration enthalpy ($\Delta H_{i,\text{hydration}}$, which is the enthalpy difference between dry and hydrous
 157 mineral phases arising from one hydrous defect, i.e., $H_{i(\text{hydrous Mgmj with one hydrous defect})}^* - NH_{\text{Mgmj}}^*$
 158 here, N has the same meaning as in R1-7), which is described in Section S1.2. $S_{i,\text{vib.}}^*$ and $S_{i,\text{conf.}}^*$ are
 159 the vibrational and configurational entropy of pure i , respectively. The former is expected to be
 160 very small and can be ignored (Muir & Brodholt, 2018; Qin et al., 2018), the latter for each phase
 161 in each reaction can be calculated from Boltzmann's entropy formula:

$$162 \quad S_{i,\text{conf.}}^* = k_B \ln W_{i,\text{conf.}} \quad (4)$$

163 where k_B is Boltzmann constant, $W_{\text{conf.}}$ represents the number of possible configurations of the
 164 hydrous defect which can be calculated from $W_{i,\text{conf.}} = C_{NV+NC}^{NV} (C_{NH+NE}^{NH})^{NV}$, where NV represents
 165 the number of defect vacancies (i.e., hydrous defects), NC represents the number of polyhedrons
 166 containing the original cation, NH represents the number of O^{2-} bonded to H^+ in vacancies and NE
 167 represents the number of O^{2-} which are not bonded to H^+ . It is obvious that this equation consists
 168 of two parts: C_{NV+NC}^{NV} is the contribution of vacancies in the lattice and $(C_{NH+NE}^{NH})^{NV}$ is the
 169 contribution of H^+ in vacancies. Due to the large number of atoms involved the former is simplified
 170 using the Stirling approximation ($\ln A! \approx A(\ln A - 1)$). For a system made of N_h unit cell of
 171 hydrous Mgmj (e.g., $\text{Mg}_{32N}\text{Si}_{32N-1}\text{O}_{96N}\text{H}_4(\text{Si1})$ in R1), assuming nv hydrous defects and nc
 172 polyhedrons containing the original cation in a unit cell (i.e., $N_h V = N_h nv$, $N_h C = N_h nc$), the
 173 $S_{i,\text{conf.}}^*$ for one unit cell can be estimated by:

$$174 \quad S_{i,\text{conf.}}^* = k_B \ln [C_{NV+NC}^{NV} (C_{NH+NE}^{NH})^{NV}] / N_h$$

$$175 \quad = \frac{k_B \ln C_{NV+NC}^{NV}}{N_h} + \frac{k_B \ln (C_{NH+NE}^{NH})^{NV}}{N_h}$$

$$\begin{aligned}
176 \quad &= \frac{k_B[(NV + NC)\ln(NV + NC) - NV\ln(NV) - NC\ln(NC)]}{N_h} + k_B\ln(C_{NH+NE}^{NH})^{nv} \\
177 \quad &= k_B[(nv + nc)\ln(nv + nc) - nv\ln(nv) - nc\ln(nc)] + k_B\ln(C_{NH+NE}^{NH})^{nv} \quad (5)
\end{aligned}$$

178 Then, at the condition of equilibrium for a balanced chemical reaction, i.e., $\Delta_r G = 0$, the Eqn.
179 (2) can be expressed as:

$$180 \quad \sum v_i(H_i^* - TS_{i,\text{conf}}^*) = -RT\ln \frac{x_{\text{Mg1}}}{x_{\text{Si1}}} \quad (6)$$

181 After solving simultaneously such equations for R1-7, we can obtain the equilibrium ratios of
182 mole fractions of seven kinds of hydrous Mgmj phases. In the Supporting Information (Section
183 S1.1 and S1.2), we provide more details of the calculation framework, including the estimation of
184 the uncertainties of our results and other technical notes.

185

186 2.2 First-principles simulations

187 First-principles simulations, which are based on a quantum mechanical description of the
188 electronic structure, are used to obtain the energy of mineral phases and the trajectories describing
189 the atomic motion used in this study. All simulations were performed with the Vienna ab initio
190 simulation package (VASP, Kresse and Hafner, 1993; Kresse and Furthmüller, 1996a, b; Kresse
191 and Joubert, 1999) which is based on density functional theory (DFT, Hohenberg and Kohn, 1964;
192 Kohn and Sham, 1965) and the projector augmented wave (PAW) approach (Blöchl, 1994; Kresse
193 & Joubert, 1999). The PBE (Perdew et al., 1996) implementation of the generalized gradient
194 approximation (GGA) to the exchange-correlation functional is used. Elements of Mg, Al, Si, O,
195 and H are included in simulations (chemical formulae are detailed in Section 2.1). The core radii
196 used by the PAW pseudopotentials were 1.06 Å for Mg ($2p^63s^2$, valence configuration with p semi-
197 core valence state), 1.01 Å for Al ($2s^22p^1$), 0.79 Å for Si ($3s^23p^2$), 0.80 Å for O ($2s^22p^4$) and 0.58
198 Å for H ($1s^1$). Van der Waals corrections were not applied in this study, since according to tests
199 by Muir and Brodholt (2018), the effect of van der Waals corrections on calculated geometry and
200 water distribution are negligible based on their comparison between DFT-D3 (Grimme et al.,
201 2010), DFT-TS (Tkatchenko & Scheffler, 2009) and non-D methods.

202 For the static simulations, the calculation parameters were: 800 eV for energy cutoff, 10^{-8} eV
203 for energy convergence criterion, and $2 \times 2 \times 2$ for the Brillouin zone sampling grid. Total energies
204 calculated with these parameters are converged to within 0.2 meV/atom. We optimized the
205 structure by minimizing the enthalpy at 0, 10, and 20 GPa. The high-temperature simulations were
206 performed by using ab initio molecular dynamics (AIMD) simulations within the NVT ensemble
207 with the Nosé thermostat (Nosé, 1984). The calculation parameters for them were: 500 eV for
208 energy cutoff, 10^{-6} eV for energy convergence criterion, and $1 \times 1 \times 1$ for the Brillouin zone sampling
209 grid (Γ -point). Total energies calculated with these parameters converged to within 1.0 meV/atom.
210 Tests show that the difference in energy obtained using a time-step, of 0.5 and 1 fs, are within 1.0
211 meV/atom and could be ignored (Table S2). Hence, each 2000 K simulation of dry and hydrous
212 Mgmj included a 1 ps pre-equilibrium stage with a 0.5 fs time-step and a 12 ps equilibrium stage
213 with a 1 fs time-step, and the systems reached equilibrium after ~ 2500 steps (Fig. S1). For other
214 minerals with a smaller unit cell, and without hydrous defects, a series of AIMD simulations were
215 used to obtain the 3rd-order Birch-Murnaghan equation of state (EOS) and the required properties

216 at the target pressure—the lack of hydrogen atoms meant that the simulation time could be shorter
217 (6 ps).

218 Initial mineral structures are built using the open-source visualization software VESTA
219 (Momma & Izumi, 2011) based on their space groups (Mgmj: Angel et al. (1989), alpha-quartz:
220 Levien et al. (1980), stishovite: Ross et al. (1990), periclase: Jacobsen et al. (2008), forsterite:
221 Hazen (1976), ringwoodite: Ye et al. (2012)) except for hydrous Mgmj. The starting structures for
222 the seven kinds of hydrous Mgmj are obtained by introducing charge-balanced substitution of H^+
223 for cations in polyhedrons in dry Mgmj. The H^+ were positioned close to several types of the O^{2-}
224 in polyhedrons based on previous static energetic simulations (Pigott et al., 2015). The pairing
225 relationships between hydrogen and oxygen ions and the bonding environments of six types of
226 oxygens are shown in Table 1. The location of hydrous defects in the lattice can be random,
227 according to Muir and Brodholt (2018). Furthermore, defect-defect interactions caused by the
228 periodic boundary conditions are considered negligible in this study as demonstrated in static
229 calculations on hydrous Mgmj (Pigott et al., 2015). The initial structures of dry and hydrous Mgmj
230 for 2000 K and ~ 20 GPa AIMD simulations are inherited from those optimized at static conditions
231 and lower pressures (the impact of imprecise pressure can be corrected as mentioned in the
232 Supplemental Section S1.2).

233 **Table 1.** The bonding environments of six types of oxygen ions in $MgSiO_3$ -majorite. The number
234 of “X” represents the number of oxygens in a polyhedron. H superscript indicates the initial
235 matching relationships between O^{2-} and H^+ in polyhedron.

Ions	Mg1 (dod)	Mg2 (dod)	Mg3 (oct)	Si1 (tet)	Si2 (tet)	Si3 (tet)	Si4 (oct)
O1	X	XX	XX			X^H	
O2	X	XX				X^H	$X^H X^H$
O3	XX					X^H	$X^H X^H$
O4	XX^H		XX			X^H	
O5	X^H	$X^H X^H$	$X^H X^H$	$X^H X^H X^H X^H$			
O6	X	XX			$X^H X^H X^H X^H$		XX

236

237

238 3 Results

239 3.1 Hydration enthalpy and configurational entropy

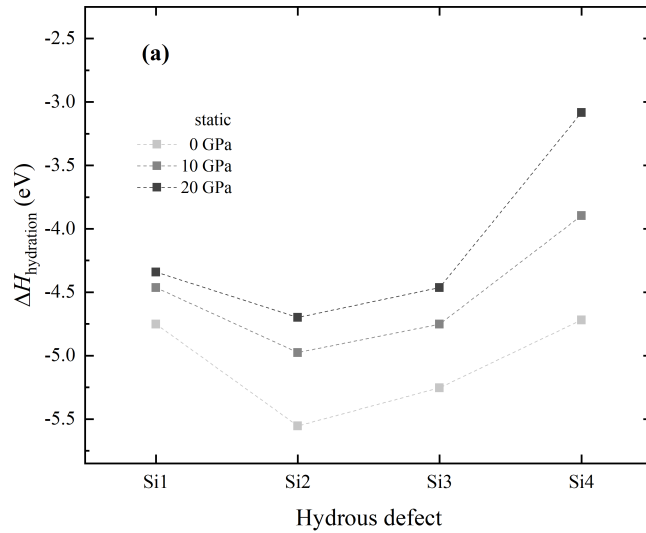
240 $\Delta H_{i,\text{hydration}}$ and $S_{i,\text{conf}}^*$ of the seven kinds of hydrous Mgmj are listed in Table 2, the $S_{i,\text{conf}}^*$
241 with water concentrations of $< \sim 5600$ ppm were determined at 2000 K because the upper limit of
242 solubility of water in Mgmj is $\sim 2200 \pm 500$ ppm (Thomas et al., 2015). There are notable
243 differences in the $\Delta H_{i,\text{hydration}}$ calculated at static conditions and 2000 K. This is because the
244 range of motion of hydrogens is larger than that of other atoms in MD simulations, which typically
245 causes a larger increase in the potential energy of hydrous Mgmj than that of dry Mgmj,
246 consequently, $\Delta H_{i,\text{hydration}}$ increases. The relative magnitude of seven $\Delta H_{i,\text{hydration}}$ remains
247 consistent from static to elevated temperatures. For Mg hydrous defects, the $\Delta H_{Mg1,\text{hydration}}$ is the
248 smallest, and its $S_{Mg1,\text{conf}}^*$ is the largest, making it the defect with the highest probability of
249 occurrence. For Si hydrous defects, the $\Delta H_{Si2,\text{hydration}}$ is the smallest (Fig. 2), however, its

250 $S_{\text{Si2,conf.}}^*$ is not the largest (being smaller than that of Si3) at the water concentrations we considered.
 251 The probability of occurrence depends on the temperature, which directly affects the contribution
 252 of S to G (the $TS_{i,\text{conf.}}^*$ term). As shown in Table 2, the $S_{\text{Si3,conf.}}^*$ of Si3 hydrous defect are always
 253 the largest among all Si hydrous defects at 2000 K. This makes its $\Delta G_{\text{Si3,hydration}}$
 254 ($\Delta H_{\text{Si3,hydration}} + TS_{\text{Si3,conf.}}^*$) is finally slightly smaller than that of Si2, resulting in the highest
 255 probability of occurrence for the Si3 hydrous defect (Fig. 2b).

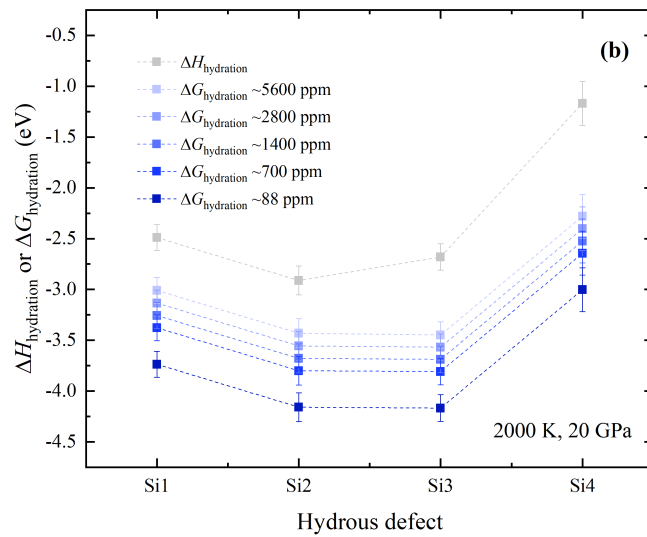
256 **Table 2.** $\Delta H_{i,\text{hydration}}$ and $S_{i,\text{conf.}}^*$ of seven kinds of hydrous Mgmj. SD represents standard
 257 deviation at 2000 K and 20 GPa.

Hydrous defect	$\Delta H_{i,\text{hydration}}$ (eV)					$S_{i,\text{conf.}}^*$ (eV/K for 4 H)				
	0 K		2000 K			Water concentration (ppm)				
	0 GPa	10 GPa	20 GPa	20 GPa	SD	~88 ppm	~700 ppm	~1400 ppm	~2800 ppm	~5600 ppm
Mg1	-1.48	-1.33	-1.29	-0.76	0.05	1.94E-03	1.58E-03	1.46E-03	1.34E-03	1.22E-03
Mg2	-1.20	-1.15	-1.25	-0.74	0.12	1.82E-03	1.46E-03	1.34E-03	1.22E-03	1.09E-03
Mg3	-1.18	-1.18	-1.30	-0.41	0.12	1.71E-03	1.35E-03	1.23E-03	1.11E-03	9.86E-04
Si1	-4.75	-4.46	-4.34	-2.49	0.07	6.24E-04	4.44E-04	3.83E-04	3.22E-04	2.60E-04
Si2	-5.55	-4.98	-4.70	-2.91	0.10	6.24E-04	4.44E-04	3.83E-04	3.22E-04	2.60E-04
Si3	-5.25	-4.75	-4.46	-2.68	0.08	7.43E-04	5.64E-04	5.04E-04	4.44E-04	3.83E-04
Si4	-4.72	-3.90	-3.08	-1.17	0.19	9.17E-04	7.37E-04	6.77E-04	6.17E-04	5.56E-04

258
 259
 260
 261
 262



263



264

265 **Figure 2.** $\Delta H_{\text{hydration}}$ and $\Delta G_{\text{hydration}}$ of Si hydrous defects for (a) static, and (b) 2000 K and 20
 266 GPa results.

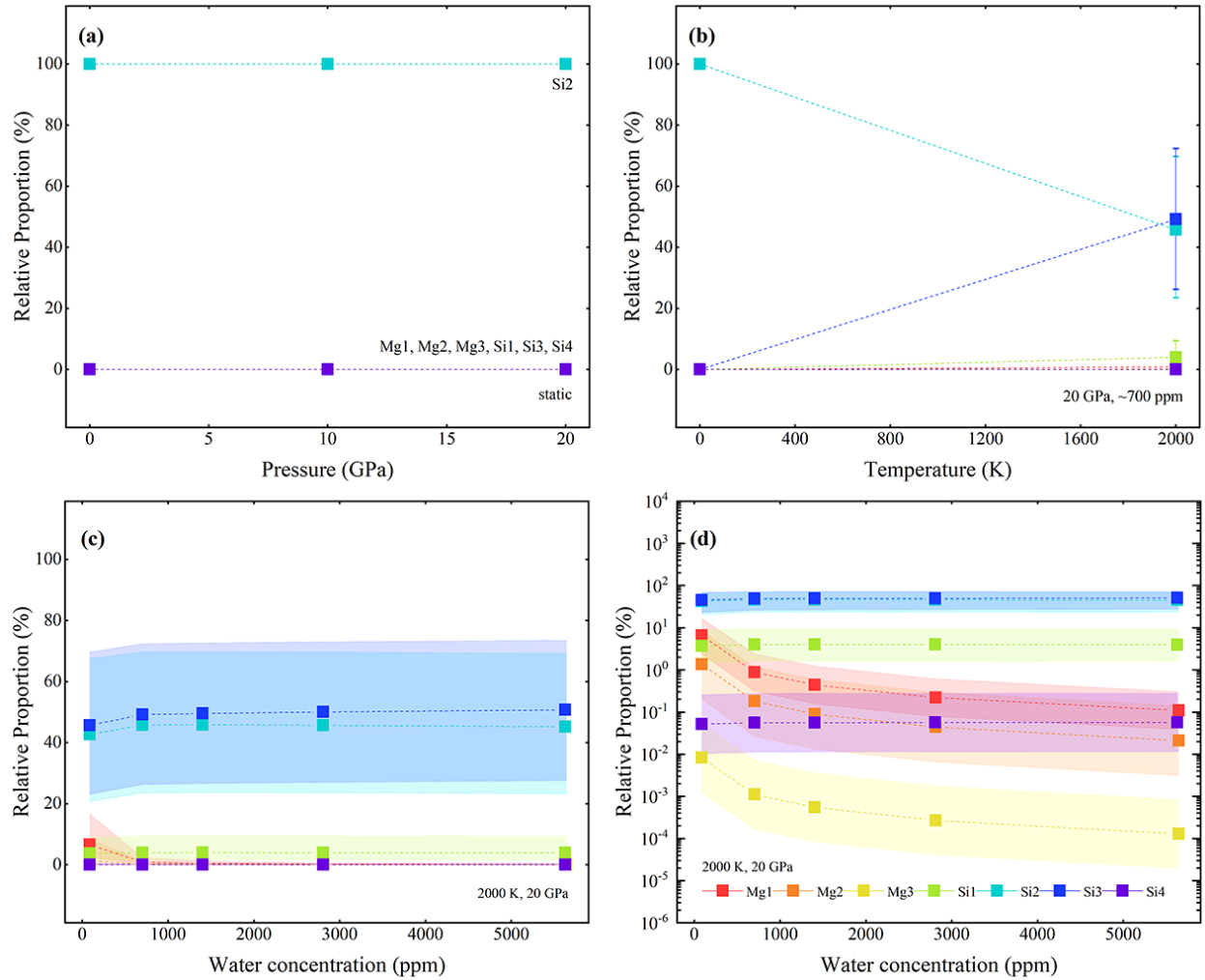
267

268 3.2 Equilibria of Reactions

269 The comparison of occurrence probability between Mg and Si hydrous defects in Mgmj relies
 270 on the ΔG for R1-7. As shown in Fig. 3a, the tetrahedral Si2 hydrous defect is the most probable
 271 hydrous defect at 0 K with almost no pressure dependence. This observation is consistent with
 272 previous ambient experimental and static simulation studies of Mgmj and other garnet phases
 273 (Bolfan-Casanova et al., 2000; Geiger et al., 1991, 2000; Katayama et al., 2003; Pigott et al., 2015).
 274 However, the ratio of another tetrahedral defect, the Si3 hydrous defect, is remarkable at high
 275 temperatures compared to static results, and it becomes the most probable hydrous defect along
 276 with Si2 hydrous defect at 2000 K and 20 GPa (Fig. 3b) with weak dependence of water
 277 concentration (Fig. 3c and d). Since the water incorporation mechanisms may be affected by the
 278 activity of SiO₂ (Lemaire et al., 2004; Matveev et al., 2001), we also calculated proportions of
 279 seven hydrous Mgmj for another set of reactions that do not contain SiO₂ (see R8-14 in Section
 280 S2.1). Comparing Fig. 3 and S3, the results seem to be quite similar, the most obvious difference
 281 is that the ratio and error of Mg1 at 88 ppm water concentration in Fig. 3c are a little larger than
 282 those in Fig S3c.

283

284



285

286 **Figure 3.** Relative proportions of seven kinds of hydrous Mgmj. (a) shows the pressure
 287 dependence at 0 K, (b) shows temperature dependence at 20 GPa, and (c) and (d) show water
 288 concentration dependence at 2000 K and 20 GPa in linear and logarithmic terms, respectively. The
 289 straight dashed lines connecting data points are guides to the eye. The confidence bands represent
 290 the estimated uncertainties in the values. Note that, except for the values for the Si2 and Si3
 291 hydrous defects, the values for all other defects are in most cases indistinguishable from the values
 292 for the Si4 hydrous defect

293

294

295

296 **4 Discussion**297 **4.1 The main water incorporation mechanism in Mgmj**

298 Our results show the dominance of Si2 and Si3 hydrous defects, while revealing the relatively
 299 small impact of pressure and water concentration on the ratios of hydrous defects. Although
 300 temperature has a more significant effect on the ratios, the trends of proportions of different
 301 hydrous defects with increasing temperature indicate that Si2 and Si3 remain predominant across
 302 the typical temperature range of Mgmj existence (T: ~1400-2000 K; Frost, 2008; Yoshizaki &
 303 McDonough, 2021). Notably, we observe binding preferences of H in hydrous defects with
 304 unsaturated pairings (i.e., Mg1, Mg2, Mg3, and Si4) in high-temperature simulations. However,
 305 this only reduces their ratios because the calculations of $S_{i,\text{conf}}^*$ assume equal binding probabilities
 306 between H and all oxygen atoms in polyhedrons. These binding preferences decreases the number
 307 of possible configurations, thereby reducing $S_{i,\text{conf}}^*$. Taking the Mg1 hydrous defect as an example,
 308 our estimation shows that when considering the binding preferences of H, the proportion of Mg1
 309 hydrous defects decreases from ~6.8% to ~3.9% at a water concentration of ~88 ppm (the condition
 310 corresponding to the largest ratio of the Mg1 hydrous defect in our results). Detailed calculations
 311 provided in Section S2.2.

312 It should also be noted that the ratios of Mg hydrous defects in our results were derived from
 313 energy calculations of hydrous Mgmj phases containing only one type of Mg hydrous defects,
 314 without considering combinations of different Mg hydrous defect types. To address this, we
 315 calculated the configurational entropy of mixed Mg hydrous defects based on the ratios of the three
 316 Mg hydrous defects (Table S3, Fig. 3c and 3d), and estimated the proportion of hydrous Mgmj
 317 phases containing three types of Mg defect at 2000 K, ~20 GPa, and a water concentration of ~88
 318 ppm conditions. The results, which do not consider binding preferences of H, show that its
 319 proportion (~12.3%) is larger than the sum of proportions of three types of hydrous Mgmj phase
 320 containing only one type of Mg hydrous defects (~8.12%). However, this difference does not affect
 321 the dominance of Si2 and Si3 defects within common water concentration ranges, i.e., at least \geq
 322 100 ppm (Section S2.3). Therefore, based on the analyses above, Si2 and Si3 hydrous defects seem
 323 to be the dominant water incorporation mechanisms in Mgmj at the conditions where Mgmj exists
 324 in the mantle (P: ~10-25 GPa; T: ~1400-2000 K; Frost, 2008; Yoshizaki & McDonough, 2021).

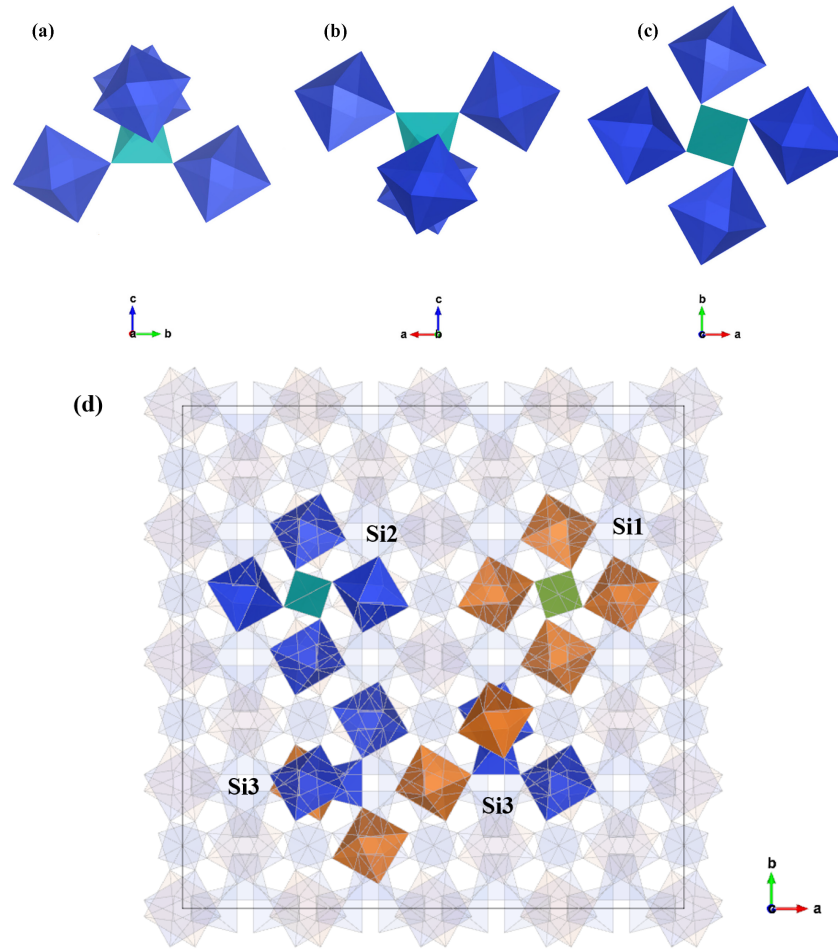
325

326 **4.2 The effects of hydrous defects**

327 The properties of hydrous Mgmj are related to the type of hydrous defects. Therefore, we
 328 compare the structure and bonding environment of three kinds of tetrahedron defects, which
 329 mainly involves two aspects, due to their expected dominance (especially Si2 and Si3) in hydrous
 330 Mgmj. The first is the types of connected octahedrons. Si1 tetrahedrons connect to four Mg
 331 octahedrons, Si2 tetrahedrons connect to four Si octahedrons, and Si3 tetrahedrons connect to two
 332 Mg octahedrons and two Si octahedrons. As shown in Table S1, the impact of a Si octahedron on
 333 the volume of Mgmj by the formation of a Si tetrahedron defect is greater than that of a Mg
 334 octahedron. In addition, the increase in the volume in hydrous Mgmj with one Si2 hydrous defect
 335 compared to dry Mgmj (about 0.86%, 0.41%, 0.22% for 0 K and 0, 10, 20 GPa, respectively) is
 336 about twice than that of Si1 (about 0.42%, 0.20%, 0.08% for 0 K and 0, 10, 20 GPa, respectively).
 337 The second is the orientation of the bonding structure. The spatial configuration of the bonding
 338 structure of Si tetrahedrons (one Si tetrahedron bonded to four octahedrons) in Mgmj is plane-like,

339 i.e., longer in two directions and shorter in the third vertical direction (see examples in Fig. 4a, b,
 340 and c). The orientation of the planar structure for Si1 and Si2 tetrahedrons are in the direction of
 341 the c-axis, but Si3 is in the direction of the a- or b-axis (Fig. 4d).

342



343

344

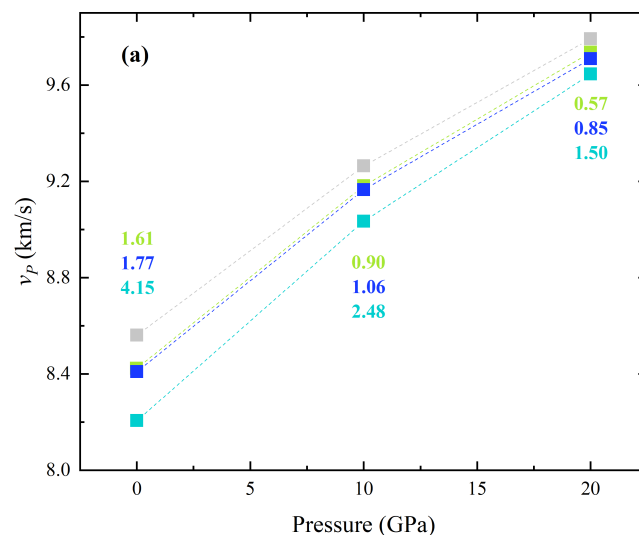
345 **Figure 4.** Sample Si tetrahedron (Si2) bonding environment: (a) front view, (b) right view, and (c)
 346 top view. And (d) is the top view of three types of sample Si tetrahedrons in a 2x2x2 supercell of
 347 Mgmj. The green tetrahedron connected with four Mg octahedrons (orange) represents Si1
 348 tetrahedron, the cyan tetrahedron connected with four Si octahedrons (blue) represents Si2
 349 tetrahedron, and the blue tetrahedron connected with two Mg octahedrons and two Si octahedrons
 350 represents Si3 tetrahedron. For clarity, other unrelated polyhedrons are made transparent and the
 351 Mg atoms in dodecahedrons are not shown.

352

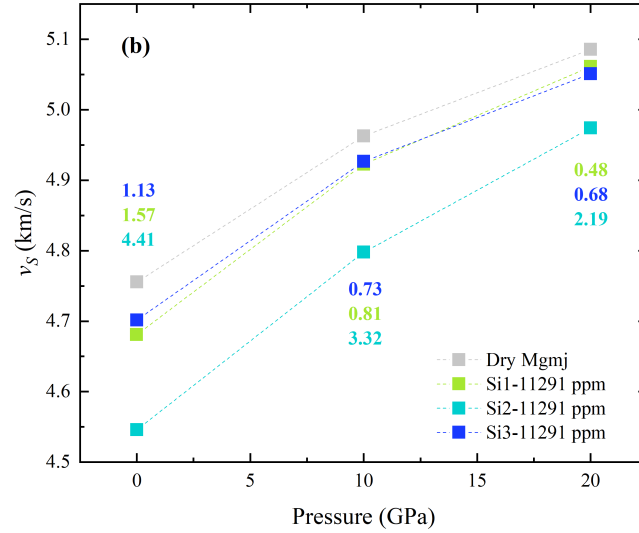
353 According to the above analysis, these three defects exert different influences on the strain of
 354 hydrous Mgmj which may be reflected in some physical properties, such as shear mechanical
 355 properties. To demonstrate this, the static seismic wave velocities for Mgmj with or without Si
 356 defects were calculated to enable comparison. The method for calculating the elastic properties
 357 followed previous studies (Lou et al., 2020; Z. Zhang et al., 2013), a detailed description is in
 358 Section S1.3. As shown in Fig. 5, S6, and S7, the reductions in elastic properties caused by

359 different hydrous defects are not the same. The decrease in most elastic constants for Si2 hydrous
 360 Mgmj compared to dry Mgmj is larger than for Si1 hydrous Mgmj (Fig. S6) due to the different
 361 types of octahedrons they connect which leads to different magnitudes of volume changes, and it
 362 also directly results in a larger reduction of K and G than that of Si1 hydrous Mgmj (Fig. S7). As
 363 for Si3 hydrous Mgmj, the magnitudes of elastic constants are higher or lower than those of Si1
 364 and Si2 hydrous Mgmj due to the combined effect of its intermediate bonding environment of two
 365 Mg and two Si octahedrons and different orientations of bonding structure (Fig. S6), which lead
 366 to a similar reduction of K and G with that of Si1 hydrous Mgmj (Fig. S7). This relative relationship
 367 of decrease in elastic modulus is carried through to seismic wave velocities because the decrease
 368 in density (e.g., about 1.59%, 1.15%, 0.97% for Si2 tetrahedron defect at 0 K and 0, 10, 20 GPa,
 369 respectively) is smaller than that in elastic moduli ($> 2\%$, see Fig. S7). Based on these, the decrease
 370 in seismic velocities v_p and v_s caused by Si1 and Si3 hydrous defects, at the same water
 371 concentrations, are almost identical and smaller than those for Si2 hydrous defects (Fig. 5). The
 372 decrease in v_p and v_s caused by the three types of Si tetrahedron defects tend to decrease with
 373 increasing pressure. This is because higher pressure results in smaller volume changes, leading to
 374 smaller variations in the elastic constants as well as bulk and shear modulus which are carried
 375 through to the seismic wave speeds. Previous studies of the elasticity of high-pressure minerals
 376 (Mao & Li, 2016) indicate the linear relationship between the water concentration and the
 377 decreases in v_p and v_s . Based on this, the decrease of v_p and v_s caused by Si2 or Si3 hydrous
 378 defect with a general water concentration of Mgmj, i.e., ~ 700 ppm (Bolfan-Casanova et al., 2000;
 379 Katayama et al., 2003; Pigott et al., 2015), at 20 GPa are about 0.09% and 0.14% or 0.05% and
 380 0.04%, respectively. Therefore, the differences in seismic wave velocities between dry and
 381 hydrous Mgmj are likely to be small in water-rich deep planetary regions, such as the MTZ in the
 382 Earth.

383



384



385

386 **Figure 5.** The variation of (a) v_P and (b) v_S caused by one Si1, Si2, and Si3 hydrous defect in
 387 MgMgJ at 0 K. The colored numbers represent the percentage of decrease compared to dry MgMgJ.

388

389 We further inspect the effects of hydrous defects on $R(\text{H}_2\text{O})$, the ratio of $d\ln(v_S)/d(\text{H}_2\text{O})$ and
 390 $d\ln(v_P)/d(\text{H}_2\text{O})$, which is a useful tool to understand lateral heterogeneities in the planetary
 391 interiors (L. Li et al., 2011; Pigott et al., 2015). Here we calculated $R(\text{H}_2\text{O})$ for MgMgJ from:

392

$$R(\text{H}_2\text{O}) = \frac{\ln v_S(\text{hydrous}) - \ln v_S(\text{anhydrous})}{\ln v_P(\text{hydrous}) - \ln v_P(\text{anhydrous})} \quad (6)$$

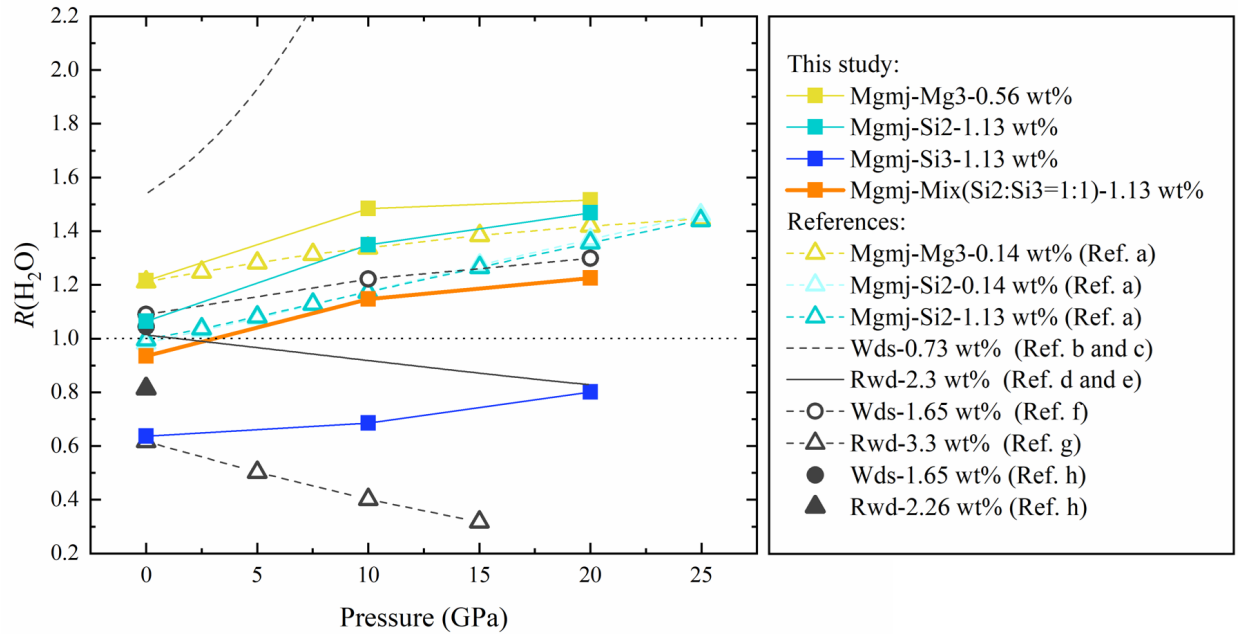
393

394 Based on this formula, a large $R(\text{H}_2\text{O})$ (> 1) indicates that v_S is more sensitive than v_P to the
 395 water concentration, whereas a small $R(\text{H}_2\text{O})$ (< 1) means the opposite is true. As shown in Fig. 6,
 396 the $R(\text{H}_2\text{O})$ of MgMgJ seems to have no dependence on water concentration which indicated by the
 397 force field (classical atomistic simulations) data of Pigott et al. (2015) of hydrous MgMgJ with Si2
 398 hydrous defects, and our results for hydrous MgMgJ with Mg3 and Si2 hydrous defects are in good
 399 agreement with their data. Since the Si3 hydrous defect is another major water incorporation
 400 mechanism, its $R(\text{H}_2\text{O})$ was also calculated. The $R(\text{H}_2\text{O})$ of Si2 and Si3 hydrous MgMgJ are different,
 401 but both of them rise with increasing pressure. We also plotted the $R(\text{H}_2\text{O})$ of wadsleyite and
 402 ringwoodite (the other two main minerals in the MTZ) using previous experimental and simulated
 403 data. Although both minerals are influenced by water concentration, their pressure-dependent
 404 trends are consistent: the $R(\text{H}_2\text{O})$ of wadsleyite increases with pressure and remains greater than
 405 1, whereas that of ringwoodite shows the opposite behavior. In comparison, the $R(\text{H}_2\text{O})$ of Si2
 406 hydrous MgMgJ is closer to those of wadsleyite, while the $R(\text{H}_2\text{O})$ of Si3 hydrous MgMgJ is similar
 407 to those of ringwoodite at lower pressure but quite different at higher pressure. Since the
 408 dominance of these two defects, the $R(\text{H}_2\text{O})$ of hydrous MgMgJ will be between their individual
 409 values and reflects the ratio of the two defects which can be applied to some areas with high MgMgJ
 410 content, such as cold subduction slab. Furthermore, the $R(\text{H}_2\text{O})$ of Si2 hydrous MgMgJ > 1 but those
 411 of Si3 < 1 , there is a cancellation effect by $R(\text{H}_2\text{O})$ of Si2 and Si3 hydrous MgMgJ. To evaluate this,
 we also estimated the $R(\text{H}_2\text{O})$ of hydrous MgMgJ with a mixture of Si2 and Si3 hydrous defects in

412 a 1:1 ratio, because the proportion of Si₃, which is about 50%, should be its upper limit due to the
413 weak pressure dependence of ratios of the hydrous defects and 2000K being the upper-temperature
414 limit of the MTZ. The values are calculated by presuming a linear relationship between water
415 concentration and seismic wave velocities (Mao & Li, 2016) and linear mixing of seismic wave
416 velocities between Si₂ and Si₃ hydrous Mgmj (Babuška et al., 1978; B. Li et al., 2022; Lou et al.,
417 2020). The results show that the $R(\text{H}_2\text{O})$ is close to 1 at low pressure but larger than 1 at high
418 pressure. Based on this, we speculate that the decrease of v_s of Mgmj caused by water is larger
419 than that of v_p in MTZ. Therefore, the effect of water on lateral variations in seismic wave
420 velocities of Mgmj is more similar to wadsleyite, but different to ringwoodite. This property could
421 be used together with others, such as the relationship between temperature and elastic properties
422 of hydrous minerals, to study the compositional heterogeneities in hydration regions in deep
423 planetary interiors like the contact zone between subducting plates and the lower MTZ of the Earth.
424 It should be noted that the discussions above are deployed from static calculations, more high-
425 temperature and high-pressure elasticity studies of hydrous Mgmj may be required to see if this is
426 also true at high temperatures.

427 Studies of other hydrous garnet end-members are also required, to better understand the effect
428 of water on lateral variations in majoritic garnets. This is because water may affect the elastic
429 properties of different garnet endmembers in distinct ways, while the major elements (e.g., Fe, Ca,
430 and Al) also exert contrasting influences on the elasticity of majoritic garnet. Specifically, under
431 MTZ pressures, Fe reduces both v_p and v_s when comparing almandine with pyrope, whereas Ca
432 and Al increase them when comparing grossular with pyrope and pyrope with majorite-pyrope
433 garnet, respectively (Fig. 5b in Liu et al. (2019)). Regarding lateral heterogeneity in seismic wave
434 velocities, as shown in Fig. S8, Fe, Ca, and Al induce larger variations in v_s than in v_p under MTZ
435 pressures. In addition, there are several points deserve further considerations: (1) the Al-related
436 mechanisms of water incorporation, such as Al-H joint substitution for Si in octahedrons or
437 tetrahedrons, and a couple of substitutions of two Al for one Mg and one Si in polyhedrons; (2)
438 comprehensive studies of the effect of SiO₂ activity on our results. Our findings in this study should
439 be of value to extend to all these more realistic circumstances.

440



442 **Figure 6.** Comparisons of the $R(\text{H}_2\text{O})$ of hydrous Mgmj and polymorphs of forsterite as a function
 443 of pressure. Ref. a: Pigott et al. (2015), static simulated data of Mgmj; Ref. b: Zha et al. (1997),
 444 experimental data only for dry wadsleyite at ambient temperature; Ref. c: Gwanmesia et al. (2020),
 445 experimental data only for hydrous wadsleyite at ambient temperature; Ref. d: B. Li (2003),
 446 experimental data only for dry ringwoodite at ambient temperature; Ref. e: Wang et al. (2006),
 447 experimental data only for hydrous ringwoodite at ambient temperature; Ref. f: Tsuchiya &
 448 Tsuchiya (2009), static simulated data of wadsleyite; Ref. g: Li et al. (2009), static simulated data
 449 of ringwoodite; Ref. h: Mao & Li (2016), ambient experimental data of wadsleyite and ringwoodite.

450 5 Conclusions

451 Our calculations provide insight into the water incorporation mechanisms in Mgmj and show
452 that (1) the Si2 hydrous defect is dominant with almost no pressure dependence at 0 K, (2) Si2 and
453 Si3 are the main hydrous defects with almost no dependence on water concentration at 2000 K and
454 20 GPa, and (3) these mechanisms are greatly affected by temperature. After evaluating the effect
455 of the binding preferences of H⁺ in defects, configurational entropy of mixed Mg hydrous defects,
456 and the sensitivities of Mg1 hydrous defects to temperature and water concentration, Si2 and Si3
457 hydrous defects are demonstrated to be the main incorporation mechanisms of water in Mgmj
458 under the Earth's and Mars' mantle conditions.

459 Our calculations also reveal the inequivalent effects of hydrous defects. The reductions of
460 seismic wave velocities caused by the Si3 hydrous defect are about half of that of the Si2 hydrous
461 defect under the same water concentration and pressure. The difference in seismic wave velocities
462 between dry and hydrous Mgmj with dominant water incorporation mechanisms (Si2 and Si3
463 hydrous defects) and expected water concentration (~700 ppm) are likely to be small (on the order
464 of one ten-thousandth). We also find that the effect of water on v_S of Mgmj is larger than that of
465 v_P based on the $R(\text{H}_2\text{O})$. Since the effect of water on lateral variations of seismic wave velocities
466 in Mgmj is opposite to that in ringwoodite, their $R(\text{H}_2\text{O})$ could be potential tools to discriminate
467 compositional heterogeneities in some hydration regions such as the contact zone between
468 subducting plates and the lower MTZ. Since the findings about elastic properties come from static
469 calculations, thus, more high-temperature and high-pressure elasticity studies of hydrous Mgmj
470 are required to see if this is also true at high temperatures. Studies of other hydrous garnet end-
471 members are also required, to better understand the effect of water on lateral variations in majoritic
472 garnets. In addition, there are several points we don't consider or investigate in detail in this study:
473 (1) the Al-related mechanisms of water incorporation, such as Al-H joint substitution for Si in
474 octahedrons or tetrahedrons, and a couple of substitutions of two Al for one Mg and one Si in
475 polyhedrons; (2) comprehensive studies of the effect of SiO₂ activity on our results. Finally, this
476 study provides inspiration and reference for the investigation of the partitioning of water between
477 high-pressure minerals, which can provide insights into the deep Earth water cycle by examining
478 how water is distributed among minerals in different layers of the Earth's interior, and our findings
479 in this study should be of value to extend to all these more realistic circumstances.

480

481 Acknowledgments

482 This work was supported by the National Key R&D Program of China (Grant
483 2022YFF0503203 and 2018YFA0702700), the key research program of IGGCAS (IGGCAS-
484 202204), the Guangdong S&T Program (2024B0303390002), the National Natural Science
485 Foundation of China (grant 92462303), the Strategic Priority Research Program of the Chinese
486 Academy of Sciences (grant XDA0430205), the Deep Earth Probe and Mineral Resources
487 Exploration — National Science and Technology Major Project of China (2024ZD1004002,
488 J.Z.), the National Key R&D Program of China (grant 2021YFC2901701), and the Science and
489 Technology Planning of Guangdong Province, China (grant 2023B1212060048). Simulations
490 were carried out on the computational facilities in the Computer Simulation Lab of IGGCAS and
491 Tianhe-2 at the National Supercomputer Center of China (NSCC) in Guangzhou. The collaboration
492 leading to this paper was made possible by the U.K.-Sino Centre for Earth and Planetary Science.

493 For the purpose of Open Access, the authors have applied a CC BY public copyright licence to
494 any Author Accepted Manuscript (AAM) version arising from this submission.
495

496 **Data Availability Statement**

497 The Vienna ab initio simulation package (VASP, Kresse & Furthmüller, 1996a, 1996b) is
498 available under the VASP license at <https://www.vasp.at/>. An open-source visualization software
499 VESTA (Momma & Izumi, 2011) used to show the crystal structures (Fig. 1 and 4) is available
500 under the VESTA license at <https://jp-minerals.org/vesta/en/>. All the data used in this study have
501 been deposited at Lou (2025).
502

503 **Conflict of Interest**

504 The authors declare that they have no conflict of interest.
505

506

507 **References**

- 508 Adhikari, P., Dharmawardhana, C. C., & Ching, W.-Y. (2017). Structure and properties of
509 hydrogrossular mineral series. *Journal of the American Ceramic Society*, *100*(9), 4317–
510 4330. <https://doi.org/10.1111/jace.14970>
- 511 Akaogi, M., & Akimoto, S. -i. (1977). Pyroxene-garnet solid-solution equilibria in the systems
512 $Mg_4Si_4O_{12}$ $Mg_3Al_2Si_3O_{12}$ and $Fe_4Si_4O_{12}$ $Fe_3Al_2Si_3O_{12}$ at high pressures and
513 temperatures. *Physics of the Earth and Planetary Interiors*, *15*(1), 90–106.
- 514 Angel, R. J., Finger, L. W., Hazen, R. M., Kanzaki, M., Weidner, D. J., Liebermann, R. C., &
515 Veblen, D. R. (1989). Structure and twinning of single-crystal $MgSiO_3$ garnet
516 synthesized at 17 GPa and 1800 C. *American Mineralogist: Journal of Earth and*
517 *Planetary Materials*, *74*(3–4), 509–512.
- 518 Babuška, V., Fiala, J., Kumazawa, M., Ohno, I., & Sumino, Y. (1978). Elastic properties of
519 garnet solid-solution series. *Physics of the Earth and Planetary Interiors*, *16*(2), 157–176.
520 [https://doi.org/10.1016/0031-9201\(78\)90086-9](https://doi.org/10.1016/0031-9201(78)90086-9)
- 521 Balan, E., Ingrin, J., Delattre, S., Kovács, I., & Blanchard, M. (2011). Theoretical infrared
522 spectrum of OH-defects in forsterite. *European Journal of Mineralogy*, *23*(3), 285–292.
523 <https://doi.org/10.1127/0935-1221/2011/0023-2090>
- 524 Bell, D. R., & Rossman, G. R. (1992). Water in Earth's mantle: The role of nominally anhydrous
525 minerals. *Science*, *255*(5050), 1391–1397.
- 526 Blanchard, M., Balan, E., & Wright, K. (2009). Incorporation of water in iron-free ringwoodite:
527 A first-principles study. *American Mineralogist*, *94*(1), 83–89.
- 528 Blöchl, P. E. (1994). Projector augmented-wave method. *Physical Review B*, *50*(24), 17953.

- 529 Bolfan-Casanova, N. (2005). Water in the Earth's mantle. *Mineralogical Magazine*, 69(3), 229–
530 257.
- 531 Bolfan-Casanova, N., Keppler, H., & Rubie, D. C. (2000). Water partitioning between nominally
532 anhydrous minerals in the MgO–SiO₂–H₂O system up to 24 GPa: Implications for the
533 distribution of water in the Earth's mantle. *Earth and Planetary Science Letters*, 182(3–
534 4), 209–221.
- 535 Cohen-Addad, C., Ducros, P., & Bertaut, E. F. (1967). Étude de la substitution du groupement
536 SiO₄ par (OH)₄ dans les composés Al₂Ca₃(OH)₁₂ et Al₂Ca₃(SiO₄)₂, 16(OH)₃, 36
537 de type grenat. *Acta Crystallographica*, 23(2), 220–230.
- 538 Faccenda, M. (2014). Water in the slab: A trilogy. *Tectonophysics*, 614, 1–30.
539 <https://doi.org/10.1016/j.tecto.2013.12.020>
- 540 Frost, D. J. (2008). The upper mantle and transition zone. *Elements*, 4(3), 171–176.
- 541 Geiger, C. A., Langer, K., Bell, D. R., Rossman, G. R., & Winkler, B. (1991). The hydroxide
542 component in synthetic pyrope. *American Mineralogist*, 76(1–2), 49–59.
- 543 Geiger, C. A., Stahl, A., & Rossman, G. R. (2000). Single-crystal IR-and UV/VIS-spectroscopic
544 measurements on transition-metal-bearing pyrope: The incorporation of hydroxide in
545 garnet. *European Journal of Mineralogy*, 12(2), 259–271.
- 546 Grimme, S., Antony, J., Ehrlich, S., & Krieg, H. (2010). A consistent and accurate ab initio
547 parametrization of density functional dispersion correction (DFT-D) for the 94 elements
548 H–Pu. *The Journal of Chemical Physics*, 132(15).
549 <https://pubs.aip.org/aip/jcp/article/132/15/154104/926936>
- 550 Gwanmesia, G. D., Whitaker, M. L., Dai, L., James, A., Chen, H., Triplett, R. S., & Cai, N.
551 (2020). The Elastic Properties of β-Mg₂SiO₄ Containing 0.73 wt.% of H₂O to 10 GPa

- 552 and 600 K by Ultrasonic Interferometry with Synchrotron X-Radiation. *Minerals*, 10(3),
553 209. <https://doi.org/10.3390/min10030209>
- 554 Hazen, R. M. (1976). Effects of temperature and pressure on the crystal structure of forsterite.
555 *American Mineralogist*, 61(11–12), 1280–1293.
- 556 Hirschmann, M., & Kohlstedt, D. (2012). Water in Earth's mantle. *Physics Today*, 65(3), 40–45.
- 557 Hohenberg, P., & Kohn, W. (1964). Inhomogeneous electron gas. *Physical Review*, 136(3B),
558 B864.
- 559 Inoue, T., Weidner, D. J., Northrup, P. A., & Parise, J. B. (1998). Elastic properties of hydrous
560 ringwoodite (γ -phase) in Mg₂SiO₄. *Earth and Planetary Science Letters*, 160(1–2), 107–
561 113.
- 562 Irifune, T. (1987). An experimental investigation of the pyroxene-garnet transformation in a
563 pyrolite composition and its bearing on the constitution of the mantle. *Physics of the*
564 *Earth and Planetary Interiors*, 45(4), 324–336.
- 565 Irifune, T., & Ringwood, A. E. (1987). Phase transformations in primitive MORB and pyrolite
566 compositions to 25 GPa and some geophysical implications. In M. H. Manghnani & Y.
567 Syono (Eds.), *Geophysical Monograph Series* (Vol. 39, pp. 231–242). American
568 Geophysical Union. <https://doi.org/10.1029/GM039p0231>
- 569 Jacobsen, S. D., Holl, C. M., Adams, K. A., Fischer, R. A., Martin, E. S., Bina, C. R., Lin, J.-F.,
570 Prakapenka, V. B., Kubo, A., & Dera, P. (2008). Compression of single-crystal
571 magnesium oxide to 118 GPa and a ruby pressure gauge for helium pressure media.
572 *American Mineralogist*, 93(11–12), 1823–1828.

- 573 Jacobsen, S. D., Jiang, F., Mao, Z., Duffy, T. S., Smyth, J. R., Holl, C. M., & Frost, D. J. (2008).
574 Effects of hydration on the elastic properties of olivine. *Geophysical Research Letters*,
575 35(14).
- 576 Katayama, I., Hirose, K., Yurimoto, H., & Nakashima, S. (2003). Water solubility in majoritic
577 garnet in subducting oceanic crust. *Geophysical Research Letters*, 30(22).
- 578 Kohn, W., & Sham, L. J. (1965). Self-consistent equations including exchange and correlation
579 effects. *Physical Review*, 140(4A), A1133.
- 580 Kresse, G., & Furthmüller, J. (1996a). Efficiency of ab-initio total energy calculations for metals
581 and semiconductors using a plane-wave basis set. *Computational Materials Science*, 6(1),
582 15–50.
- 583 Kresse, G., & Furthmüller, J. (1996b). Efficient iterative schemes for ab initio total-energy
584 calculations using a plane-wave basis set. *Physical Review B*, 54(16), 11169.
- 585 Kresse, G., & Hafner, J. (1993). Ab initio molecular dynamics for liquid metals. *Physical Review*
586 *B*, 47(1), 558.
- 587 Kresse, G., & Joubert, D. (1999). From ultrasoft pseudopotentials to the projector augmented-
588 wave method. *Physical Review B*, 59(3), 1758.
- 589 Lemaire, C., Kohn, S. C., & Brooker, R. A. (2004). The effect of silica activity on the
590 incorporation mechanisms of water in synthetic forsterite: A polarised infrared
591 spectroscopic study. *Contributions to Mineralogy and Petrology*, 147, 48–57.
- 592 Levien, L., Prewitt, C. T., & Weidner, D. J. (1980). Structure and elastic properties of quartz at
593 pressure. *American Mineralogist*, 65(9–10), 920–930.
- 594 Levine, I. N. (2009). *Physical chemistry* (6th ed). McGraw-Hill.

- 595 Li, B. (2003). Compressional and shear wave velocities of ringwoodite γ -Mg₂SiO₄ to 12 GPa.
596 *American Mineralogist*, 88(8–9), 1312–1317. <https://doi.org/10.2138/am-2003-8-913>
- 597 Li, B., Jiang, J., Xu, J., Tkachev, S. N., Ye, Z., Huang, S., Guo, W., Zeng, Y., Prakapenka, V. B.,
598 Fan, D., & Zhou, W. (2022). Effect of Thermoelastic Properties of the Pyrope-Almandine
599 Solid Solutions on the Entrapment Pressure of Garnet-Related Elastic Geobarometer.
600 *Frontiers in Earth Science*, 9.
601 <https://www.frontiersin.org/articles/10.3389/feart.2021.833405>
- 602 Li, L., Brodholt, J., & Alfè, D. (2009). Structure and elasticity of hydrous ringwoodite: A first
603 principle investigation. *Physics of the Earth and Planetary Interiors*, 177(3–4), 103–115.
- 604 Li, L., Weidner, D. J., Brodholt, J. P., & Alfè, D. (2011). Prospecting for water in the transition
605 zone: $D \ln(V_s)/d \ln(V_p)$. *Physics of the Earth and Planetary Interiors*, 189(1–2), 117–
606 120.
- 607 Liu, Z., Gréaux, S., Cai, N., Siersch, N., Ballaran, T. B., Irifune, T., & Frost, D. J. (2019).
608 Influence of aluminum on the elasticity of majorite-pyrope garnets. *American*
609 *Mineralogist*, 104(7), 929–935. <https://doi.org/10.2138/am-2019-6771>
- 610 Lou, Y. (2025). *Water Incorporation Mechanisms and Effects in MgSiO₃-majorite Under High*
611 *Temperature and Pressure Conditions* [Dataset].
612 <https://doi.org/10.5281/zenodo.17406948>
- 613 Lou, Y., Stackhouse, S., Walker, A. M., & Zhang, Z. (2020). Thermoelastic properties of
614 MgSiO₃-majorite at high temperatures and pressures: A first principles study. *Physics of*
615 *the Earth and Planetary Interiors*, 303, 106491.
616 <https://doi.org/10.1016/j.pepi.2020.106491>

- 617 Manghnani, M. H., Amulele, G., Smyth, J. R., Holl, C. M., Chen, G., Prakapenka, V., & Frost,
618 D. J. (2005). Equation of state of hydrous Fo90 ringwoodite to 45 GPa by synchrotron
619 powder diffraction. *Mineralogical Magazine*, 69(3), 317–323.
- 620 Mao, Z., Jacobsen, S. D., Frost, D. J., McCammon, C. A., Hauri, E. H., & Duffy, T. S. (2011).
621 Effect of hydration on the single-crystal elasticity of Fe-bearing wadsleyite to 12 GPa.
622 *American Mineralogist*, 96(10), 1606–1612.
- 623 Mao, Z., & Li, X. (2016). Effect of hydration on the elasticity of mantle minerals and its
624 geophysical implications. *Science China Earth Sciences*, 59, 873–888.
- 625 Matveev, S., O’neill, H. S. C., Ballhaus, C., Taylor, W. R., & Green, D. H. (2001). Effect of
626 silica activity on OH- IR spectra of olivine: Implications for low- a SiO₂ mantle
627 metasomatism. *Journal of Petrology*, 42(4), 721–729.
- 628 Momma, K., & Izumi, F. (2011). VESTA 3 for three-dimensional visualization of crystal,
629 volumetric and morphology data. *Journal of Applied Crystallography*, 44(6), 1272–1276.
630 <https://doi.org/10.1107/S0021889811038970>
- 631 Muir, J. M. R., & Brodholt, J. P. (2018). Water distribution in the lower mantle: Implications for
632 hydrolytic weakening. *Earth and Planetary Science Letters*, 484, 363–369.
633 <https://doi.org/10.1016/j.epsl.2017.11.051>
- 634 Nestola, F., & Smyth, J. R. (2016). Diamonds and water in the deep Earth: A new scenario.
635 *International Geology Review*, 58(3), 263–276.
636 <https://doi.org/10.1080/00206814.2015.1056758>
- 637 Ni, H., Zheng, Y.-F., Mao, Z., Wang, Q., Chen, R.-X., & Zhang, L. (2017). Distribution, cycling
638 and impact of water in the Earth’s interior. *National Science Review*, 4(6), 879–891.
639 <https://doi.org/10.1093/nsr/nwx130>

- 640 Nosé, S. (1984). A molecular dynamics method for simulations in the canonical ensemble.
641 *Molecular Physics*, 52(2), 255–268.
- 642 Ohtani, E. (2020). The role of water in Earth’s mantle. *National Science Review*, 7(1), 224–232.
- 643 Pearson, D. G., Brenker, F. E., Nestola, F., McNeill, J., Nasdala, L., Hutchison, M. T., Matveev,
644 S., Mather, K., Silversmit, G., Schmitz, S., Vekemans, B., & Vincze, L. (2014). Hydrous
645 mantle transition zone indicated by ringwoodite included within diamond. *Nature*,
646 507(7491), Article 7491. <https://doi.org/10.1038/nature13080>
- 647 Perdew, J. P., Burke, K., & Ernzerhof, M. (1996). Generalized gradient approximation made
648 simple. *Physical Review Letters*, 77(18), 3865.
- 649 Peslier, A. H., Schönbacher, M., Busemann, H., & Karato, S.-I. (2017). Water in the Earth’s
650 Interior: Distribution and Origin. *Space Science Reviews*, 212(1), 743–810.
651 <https://doi.org/10.1007/s11214-017-0387-z>
- 652 Pigott, J. S., Wright, K., Gale, J. D., & Panero, W. R. (2015). Calculation of the energetics of
653 water incorporation in majorite garnet. *American Mineralogist*, 100(5–6), 1065–1075.
- 654 Qin, T., Wentzcovitch, R. M., Umemoto, K., Hirschmann, M. M., & Kohlstedt, D. L. (2018). Ab
655 initio study of water speciation in forsterite: Importance of the entropic effect. *American*
656 *Mineralogist*, 103(5), Article 5.
- 657 Ringwood, A. E. (1967). The pyroxene-garnet transformation in the earth’s mantle. *Earth and*
658 *Planetary Science Letters*, 2(3), 255–263.
- 659 Ringwood, A. E. (1991). Phase transformations and their bearing on the constitution and
660 dynamics of the mantle. *Geochimica et Cosmochimica Acta*, 55(8), 2083–2110.
- 661 Ross, N. L., Shu, J., & Hazen, R. M. (1990). High-pressure crystal chemistry of stishovite.
662 *American Mineralogist*, 75(7–8), 739–747.

- 663 Rossman, G. R., & Aines, R. D. (1991). The hydrous components in garnets: Grossular-
664 hydrogrossular. *American Mineralogist*, *76*(7–8), 1153–1164.
- 665 Scambelluri, M., Pettke, T., & van Roermund, H. L. M. (2008). Majoritic garnets monitor deep
666 subduction fluid flow and mantle dynamics. *Geology*, *36*(1), 59–62.
667 <https://doi.org/10.1130/G24056A.1>
- 668 Smith, E. M., Shirey, S. B., Richardson, S. H., Nestola, F., Bullock, E. S., Wang, J., & Wang, W.
669 (2018). Blue boron-bearing diamonds from Earth’s lower mantle. *Nature*, *560*(7716), 84–
670 87. <https://doi.org/10.1038/s41586-018-0334-5>
- 671 Smyth, J. R., & Jacobsen, S. D. (2006). Nominally anhydrous minerals and Earth’s deep water
672 cycle. *Earth’s Deep Water Cycle*, *168*, 1–11.
- 673 Stixrude, L., & Lithgow-Bertelloni, C. (2012). Geophysics of Chemical Heterogeneity in the
674 Mantle. *Annual Review of Earth and Planetary Sciences*, *40*(1), 569–595.
675 <https://doi.org/10.1146/annurev.earth.36.031207.124244>
- 676 Thomas, S.-M., Wilson, K., Koch-Müller, M., Hauri, E. H., McCammon, C., Jacobsen, S. D.,
677 Lazarz, J., Rhede, D., Ren, M., & Blair, N. (2015). Quantification of water in majoritic
678 garnet. *American Mineralogist*, *100*(5–6), 1084–1092.
- 679 Tkatchenko, A., & Scheffler, M. (2009). Accurate Molecular Van Der Waals Interactions from
680 Ground-State Electron Density and Free-Atom Reference Data. *Physical Review Letters*,
681 *102*(7), 073005. <https://doi.org/10.1103/PhysRevLett.102.073005>
- 682 Tsuchiya, J., & Tsuchiya, T. (2009). First principles investigation of the structural and elastic
683 properties of hydrous wadsleyite under pressure. *Journal of Geophysical Research: Solid*
684 *Earth*, *114*(B2).

- 685 van der Lee, S. (2023). Deep Mars is surprisingly soft. *Nature*, 622(7984), 699–700.
686 <https://doi.org/10.1038/d41586-023-03151-x>
- 687 van Mierlo, W. L., Langenhorst, F., Frost, D. J., & Rubie, D. C. (2013). Stagnation of subducting
688 slabs in the transition zone due to slow diffusion in majoritic garnet. *Nature Geoscience*,
689 6(5), 400–403. <https://doi.org/10.1038/ngeo1772>
- 690 Walker, A. M., Hermann, J., Berry, A. J., & O'Neill, H. S. C. (2007). Three water sites in upper
691 mantle olivine and the role of titanium in the water weakening mechanism. *Journal of*
692 *Geophysical Research: Solid Earth*, 112(B5).
- 693 Wang, J., Sinogeikin, S. V., Inoue, T., & Bass, J. D. (2006). Elastic properties of hydrous
694 ringwoodite at high-pressure conditions. *Geophysical Research Letters*, 33(14).
- 695 Wright, K., Freer, R., & Catlow, C. R. A. (1994). The energetics and structure of the hydrogarnet
696 defect in grossular: A computer simulation study. *Physics and Chemistry of Minerals*,
697 20(7), 500–503. <https://doi.org/10.1007/BF00203220>
- 698 Ye, Y., Brown, D. A., Smyth, J. R., Panero, W. R., Jacobsen, S. D., Chang, Y.-Y., Townsend, J.
699 P., Thomas, S.-M., Hauri, E. H., & Dera, P. (2012). Compressibility and thermal
700 expansion of hydrous ringwoodite with 2.5 (3) wt% H₂O. *American Mineralogist*, 97(4),
701 573–582.
- 702 Yoshizaki, T., & McDonough, W. F. (2020). The composition of Mars. *Geochimica et*
703 *Cosmochimica Acta*, 273, 137–162. <https://doi.org/10.1016/j.gca.2020.01.011>
- 704 Yoshizaki, T., & McDonough, W. F. (2021). Earth and Mars – Distinct inner solar system
705 products. *Geochemistry*, 81(2), 125746. <https://doi.org/10.1016/j.chemer.2021.125746>

- 706 Zha, C., Duffy, T. S., Mao, H., Downs, R. T., Hemley, R. J., & Weidner, D. J. (1997). Single-
707 crystal elasticity of β -Mg₂SiO₄ to the pressure of the 410 km seismic discontinuity in the
708 earth's mantle. *Earth and Planetary Science Letters*, 147(1–4), E9–E15.
- 709 Zhang, B., & Xia, Q. (2021). Influence of water on the physical properties of olivine, wadsleyite,
710 and ringwoodite. *European Journal of Mineralogy*, 33(1), 39–75.
711 <https://doi.org/10.5194/ejm-33-39-2021>
- 712 Zhang, Z., Stixrude, L., & Brodholt, J. (2013). Elastic properties of MgSiO₃-perovskite under
713 lower mantle conditions and the composition of the deep Earth. *Earth and Planetary
714 Science Letters*, 379, 1–12.
- 715
716